PHOTONICS Research

Butler matrix enabled multi-beam optical phased array for two-dimensional beam-steering and ranging

Zuoyu Zhou,[1,2,†] Weihan Xu,[1,†] Chuxin Liu,[1] Ruiyang Xu,[1] Chen Zhu,[1] Xinhang Li,[1] Liangjun Lu,[1,3,*] Jianping Chen,[1,3] and Linjie Zhou[1,3]

[1]State Key Laboratory of Advanced Optical Communication Systems and Networks, Shanghai Key Laboratory of Navigation and Location Services, Shanghai Institute for Advanced Communication and Data Science, Department of Electronic Engineering, Shanghai Jiao Tong University, Shanghai 200240, China
[2]SJTU-Pinghu Institute of Intelligent Optoelectronics, Pinghu 314200, China
[3]State Grid Sichuan Electric Power Company Chengdu Xinjin Power Supply Branch, Xinjin 611430, China
[†]These authors contributed equally to this work.
*Corresponding author: luliangjun@sjtu.edu.cn

Received 18 October 2023; revised 7 February 2024; accepted 25 February 2024; posted 26 February 2024 (Doc. ID 509595); published 26 April 2024

Based on the wavelength transparency of the Butler matrix (BM) beamforming network, we demonstrate a multi-beam optical phased array (MOPA) with an emitting aperture composed of grating couplers at a 1.55 μm pitch for wavelength-assisted two-dimensional beam-steering. The device is capable of simultaneous multi-beam operation in a field of view (FOV) of 60° × 8° in the phased-array scanning axis and the wavelength-tuning scanning axis, respectively. The typical beam divergence is about 4° on both axes. Using multiple linearly chirped lasers, multi-beam frequency-modulated continuous wave (FMCW) ranging is realized with an average ranging error of 4 cm. A C-shaped target is imaged for proof-of-concept 2D scanning and ranging.

https://doi.org/10.1364/PRJ.509595

1. INTRODUCTION

With the vigorous development of photonic integrated circuits (PICs) and solid-state LiDARs, chip-scale optical phased arrays (OPAs) have received increased attention [1–13] for their seamless yet inertia-free optical beam scanning. OPAs hold promise for software-defined LiDARs where both beam scanning and beam patterns can be reconfigured adaptively and digitally. Meanwhile, with the real-time requirements in practical applications such as autonomous driving, multi-beam solutions have been widely adopted. The introduction of parallel multi-beam scanning divides the desired field of view (FOV) into multiple sub-sectors, each covering a smaller solid angle. This multiplies the sampling rate, enabling a higher refresh rate at the original spatial resolution. Moreover, this technology is especially beneficial for frequency-modulated continuous wave (FMCW) ranging, where the repetition rate of the chirped signal limits the point rate.

In recent years, a significant amount of effort [14–19] has been devoted to enabling the multi-beam operation in chip-scale OPAs—either with multi-periods grating couplers [15], sub-aperture methods [16,17], amplitude-phase cascade methods [18], iterative Fourier transforms method [19], or power distribution networks [20]. Previously, we demonstrated a one-dimensional (1D) multi-beam OPA based on a 4 × 4 Butler matrix (BM) [21]. To further exploit the wavelength transparency of the beamforming network, we implement an emitting aperture composed of grating antennas with a 1.55 μm pitch for wavelength-assisted two-dimensional (2D) beam-steering. Simultaneous multi-beam ranging of multiple wavelengths is demonstrated through a shared aperture, realizing the imaging of the C-shaped target.

2. STRUCTURE DESIGN AND WAVELENGTH TRANSPARENCY VALIDATION

A. Device Structure

Figure 1(a) shows the schematic of the BM-based multi-beam OPA (MOPA) chip consisting of a 4 × 4 BM, a 4 × 16 power distribution network, a 16-channel phase shifter, and a grating array for emitting antennas. Figure 1(b) shows the structure of the 4 × 4 BM, which contains four input ports based on grating couplers, four 3 dB couplers based on 2 × 2 multi-mode interferometers (MMIs) interlinked with a waveguide crossing to shuffle the outputs of the first stage, two phase shifters for active phase alignment, and four output ports connecting to the following power distribution stages where the middle two outputs are shuffled once more. When light is injected into one of the

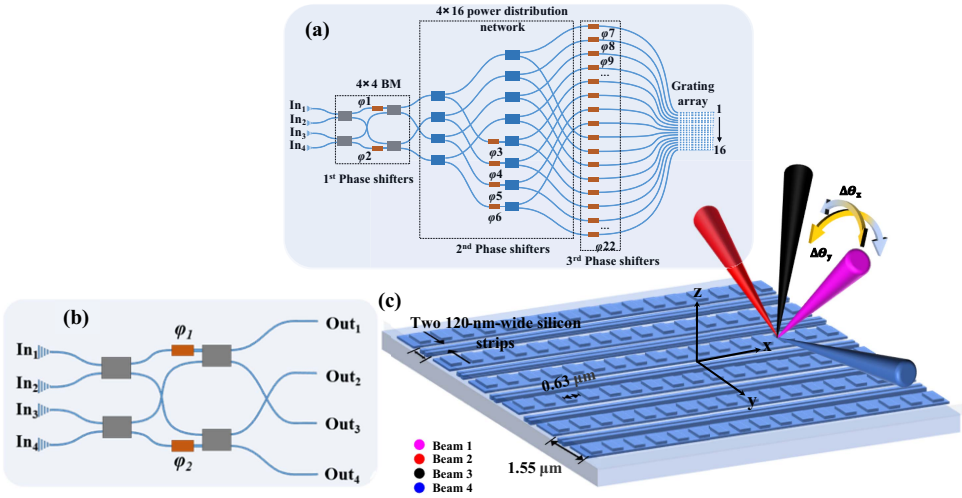

Fig. 1. (a) Schematic of the 4 × 4 Butler MOPA chip. (b) Detailed illustration of the 4 × 4 BM with the corresponding port labels. (c) Schematic diagram of the emitting grating coupler.

input ports, the optical power is distributed evenly among the four output ports. Besides, inside the 4 × 4 BM, when the phase difference between the straight connection and the crossed connection (φ_1 and φ_4) is $\pi/4$, a linearly progressive phase difference between the four output ports is obtained when light is injected from each input port. Table 1 summarizes the phase difference for these four input ports, which are $\pm\pi/4$ from In_1/In_4, and $\pm 3\pi/4$ from In_3/In_2. We have detailed the input-dependent phase response of the BM beamforming network in Ref. [21].

The following 4 × 16 power distribution network consists of two stages of 1 × 2 MMI couplers from each output port of the 4 × 4 BM. It maintains the inter-channel phase difference determined by the 4 × 4 BM through shuffling waveguide connections and phase adjustment of φ_3–φ_6. As a result, four beams are generated and pointed in different directions through a shared aperture when light is launched into the four input ports. The 16-channel phase shifter, followed by the power distribution stage, introduces an additional phase differential to tilt the phase front of the aperture, thereby rotating the four beams simultaneously. As shown in Fig. 1(a), there are 22 phase shifters in the chip. All the phase shifters are based on the thermo-optic (TO) effect. Finally, light is emitted by the grating-based antennas for beamforming in free space. Four beams are generated in the far field when light is injected from In_1 to In_4, referred to as beam1, beam2, beam3, and beam4, respectively.

Figure 1(c) shows the structure of the emitting aperture adopted in this paper. It consists of 16 shallowly etched silicon gratings arranged at a pitch of 1.55 μm. The grating period is 0.63 μm, the etching depth is 70 nm, the duty cycle is 50%, and the total size of the aperture is 0.024 mm × 0.032 mm in the lateral (x) and longitudinal (y) directions. At an operating wavelength of 1.55 μm, the simulated beam divergence characterized w.r.t. the full width at half maximum (FWHM) of the intensity distribution is 3.10° × 4.32° ($\Delta\theta_x \times \Delta\theta_y$). Meanwhile, the aliasing-free FOV in the phased-array scanning axis (x) is ±30°, the emitting angle of the grating antenna (y) is at 12° at the 1550 nm wavelength, and the wavelength-scanning efficiency is 0.13 deg/nm. Moreover, two silicon strips with a width of 120 nm and an interval of 120 nm are inserted between two adjacent gratings [22,23] to suppress the crosstalk between gratings.

Table 1. Constant Phase Difference among the Outputs with Respect to Each Input Port

Port	In_1	In_2	In_3	In_4
Out_1	$\pi/4$	$3\pi/4$	$\pi/2$	π
Out_2	$\pi/2$	0	$5\pi/4$	$3\pi/4$
Out_3	$3\pi/4$	$5\pi/4$	0	$\pi/2$
Out_4	π	$\pi/2$	$3\pi/4$	$\pi/4$
Phase difference (rad)	$\pi/4$	$-3\pi/4$	$3\pi/4$	$-\pi/4$

B. Wavelength Transparency Validation

The wavelength transparency of conventional 1D OPAs has been validated; thereby, 2D OPAs assisted by tunable laser wavelength and grating arrays have been widely adopted. For our BM-based MOPA chip, the input wavelength-dependent phase response should hold over a large optical bandwidth, permitting wavelength-assisted 2D scanning. Since the phased array is wavelength transparent, it is important to demonstrate that the BM is also wavelength transparent. Therefore, the wavelength scanning in the optical band near the designed operating wavelength will not affect the beam quality of the multibeam pattern. Since the 4 × 4 BM consists of MMIs, TO phase shifters, and waveguide connections of equal optical path lengths, we validate the dispersion characteristics of each component shown in Fig. 1(b) and incorporate wavelength-related phase shifts of the MMIs and TO phase shifters in a transmission matrix model to verify the wavelength transparency of the entire device.

To begin with, we simulate the transmission characteristics of the 2 × 2 MMI with the three-dimensional (3D) finite-difference time-domain (FDTD) method. The design is optimized for power uniformity between the output ports and low insertion loss according to the self-imaging theory [24,25],

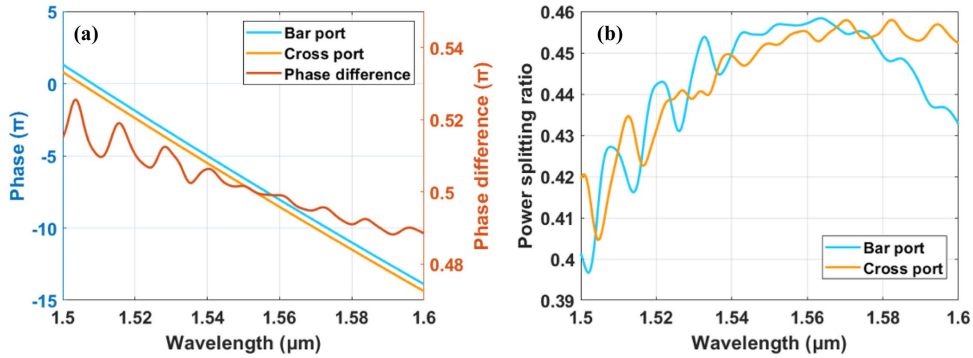

Fig. 2. (a) Phase response and (b) power splitting ratio of the 2 × 2 MMI output ports. The blue and orange lines indicate the bar and cross ports, respectively.

while the inter-port phase difference is analyzed emphatically. More specifically, since the device is laterally symmetric, the phase response of the upper port can be mirrored onto the lower port. For either input port, the parallel output port (i.e., the bar port) leads the diagonal output port (i.e., the cross port) with a wavelength-dependent phase shift. We verify this phase shift in the optical band from 1500 to 1600 nm. As shown in Fig. 2(a), the phase on the cross port lags behind that of the bar port by about 0.5π. The exact phase differences are retrieved and modeled into the transmission matrix of the 2 × 2 MMIs. For example, we showcase phase differences at five wavelengths in Table 2. Note that the power distribution and the insertion loss are wavelength dependent for the aforementioned power-splitting components. Though amplitude variations do not undermine the condition for constructive interference, they also contribute to the device's beam quality, namely, the side-lobe suppression ratio (SLSR). Therefore, the transmission matrix also modeled the amplitude response according to the complex transmission coefficients of both MMIs. Here, we showcase an amplitude response of the 2 × 2 MMI in Fig. 2(b) and Table 2.

We validate the 1 × 2 MMI in the device similarly. However, the phase difference remains zero across the wavelength band since both output ports are symmetric w.r.t. the input port. For other passive components, such as waveguide crossings and interconnecting waveguides, we compensate for the geometric length and the number of crossings on each path to ensure equal optical path length and insertion loss in our design. Therefore, other passive components' dispersions (wavelength-dependent amplitude and phase responses) cancel out among each other and are omitted from the transmission matrix model.

To validate the wavelength dependency of the TO phase shifter, we perform a 2D parametric sweep over the operating wavelength (λ) and the heating power (ΔP) based on the refractive indices of the silicon and silica at the corresponding wavelengths and temperatures [26]. By solving effective indices (n_{eff}) of the waveguide based on the aforementioned refractive indices, the corresponding phase shifts ($\Delta\varphi$) in a phase shifter of length (L) are therefore derived as

$$\Delta n_{\text{eff}} = n_{\text{eff}}(\Delta P, \lambda), \tag{1}$$

$$\Delta\varphi = k_0 \times \Delta n_{\text{eff}} \times L, \tag{2}$$

where $k_0 = 2\pi/\lambda$ is the wavenumber. By retrieving the effective indices at a different wavelength, Eqs. (1) and (2) can be employed to validate the wavelength transparency at a fixed heating power (ΔP). The result of the 2D parametric sweep is represented in Fig. 3. It is worth noting that within the simulated C-band, the phase shift is highly dependent on the heating power while the deviation in phase shift is below 0.42π.

For practical evaluation of the entire device, we introduced randomly generated phase errors to individual waveguide connections following a normal distribution. The distribution is centered at 0 rad with a standard deviation of π rad. We simulate the phase alignment of the device at 1550 nm to generate the look-up table of TO phase shifters. Therefore, each phase shifter is designated with heating power according to the beamforming condition at the central wavelength. By incorporating the wavelength dependency analysis of all components mentioned above in the transmission matrix model, the wavelength

Table 2. Phase Difference between the Two Outputs and Power Splitting Ratio of the 2 × 2 MMI

Wavelength (nm)		1510	1530	1550	1570	1590
Power splitting ratio	Cross	0.426	0.447	0.456	0.455	0.442
	Bar	0.427	0.439	0.452	0.458	0.453
Phase difference (rad)		1.601	1.605	1.576	1.555	1.535

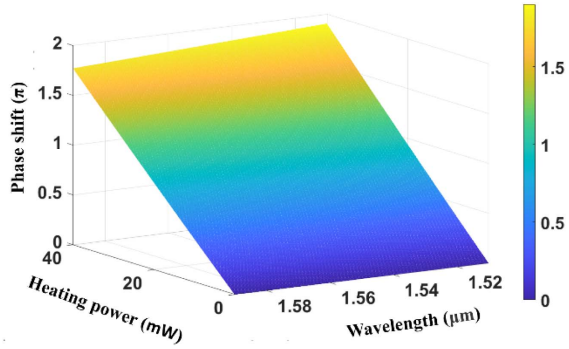

Fig. 3. Phase response of the TO phase shifter w.r.t. heating power and operating wavelength.

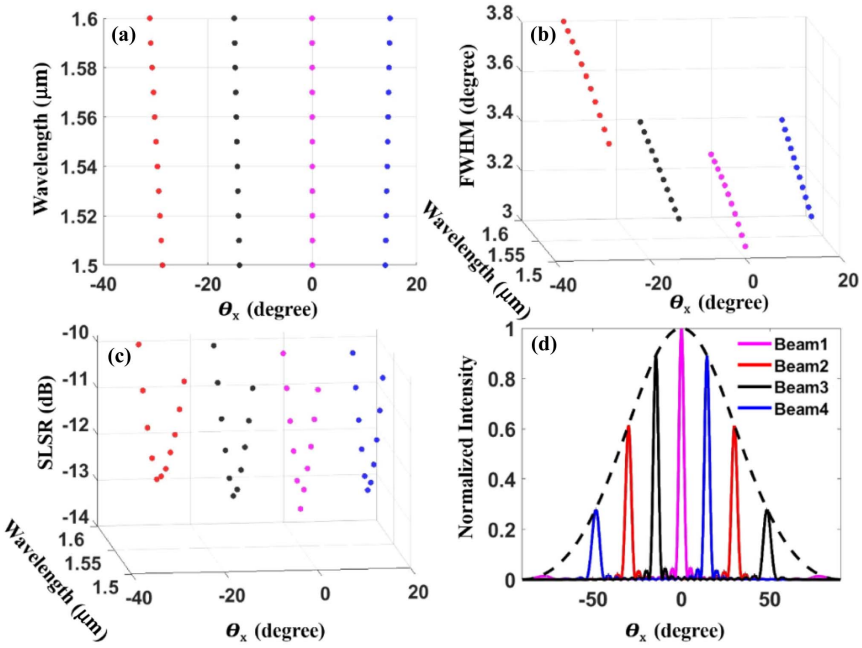

Fig. 4. Results of wavelength transparency simulation when the laser wavelength of the OPA is adjusted sequentially from 1.5 to 1.6 μm in 0.01 μm steps. (a) Distribution of simulated peak directions, (b) FWHM, and (c) SLSR of each beam of the multi-beam OPA, with pink, red, black, and blue points representing beams from In_1, In_2, In_3, and In_4 in simulation. (d) Far-field intensity distribution of the multi-beam pattern after beamforming at the central operating wavelength of 1.55 μm.

transparency of the entire device is validated in the form of multi-beam patterns and their beam quality, as shown in Fig. 4. The far-field interference pattern of the elements is obtained based on the Fraunhofer diffraction equation for isotropic point sources. The emitting angle in the lateral/phased-array-scanning direction (θ_x), the SLSR, and the beam divergence measured in FWHM are characterized for beam quality. Note that the lobe pattern for In_2/beam2 is aliased at ±30°, corresponding to the 1.55 μm element pitch of the emitting aperture. The SLSR is measured for the −30° lobe w.r.t. its nearest side lobe. Based on the simulated results, it is evident that the multi-beam OPA maintains a precise beam direction and beam divergence from 1500 to 1600 nm with nearly identical behavior compared to the standard wavelength-assisted OPAs. Additionally, based on the SLSR, the device has a 3 dB optical bandwidth of ∼100 nm, which is dominated by the standard deviation value of the phase error distribution. In conclusion, the wavelength transparency will hold for a practical device with small processing errors.

3. EXPERIMENTAL VERIFICATION

The MOPA chip [27] was fabricated on an 8-inch SOI wafer with a 220-nm-thick silicon layer and a 3-μm-thick buried oxide layer. The chip footprint is 3.5 mm × 2.1 mm. The chip was first wire-bonded to a printed circuit board (PCB). Then, a 45° polished fiber array (FA) was aligned to the four input grating couplers of the chip and fixed by UV-curable adhesive. Figure 5 shows the microscope image of the packaged chip. We used four distributed feedback (DFB) lasers to launch light into the input ports, and a multi-channel voltage source was used to drive the phase shifters of the MOPA chip.

We used a Fourier imaging system calibrated for far-field imaging to capture the far-field pattern from the 2D MOPA. Based on the feedback from the camera, the voltage applied to the TO phase shifter is optimized for the phase alignment of the device. Figure 6 shows the experimental setup. The far-field calibration shows that the maximum effective FOV is about 60°. For the phase alignment of the MOPA chip, we employed an optimization algorithm combining a sequential

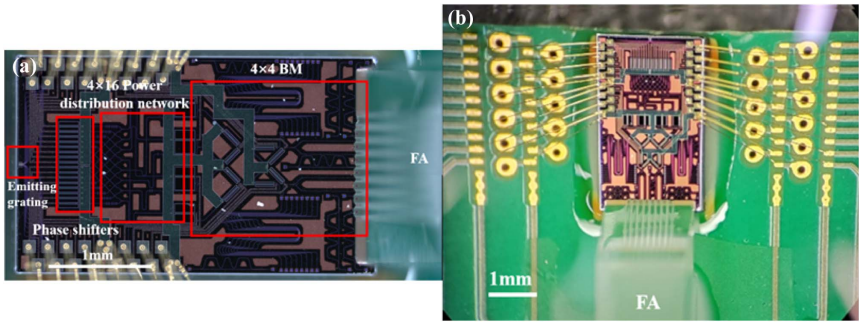

Fig. 5. (a) Microscope image of the chip after packaging. (b) Picture of the packaged chip, including the PCB and the FA.

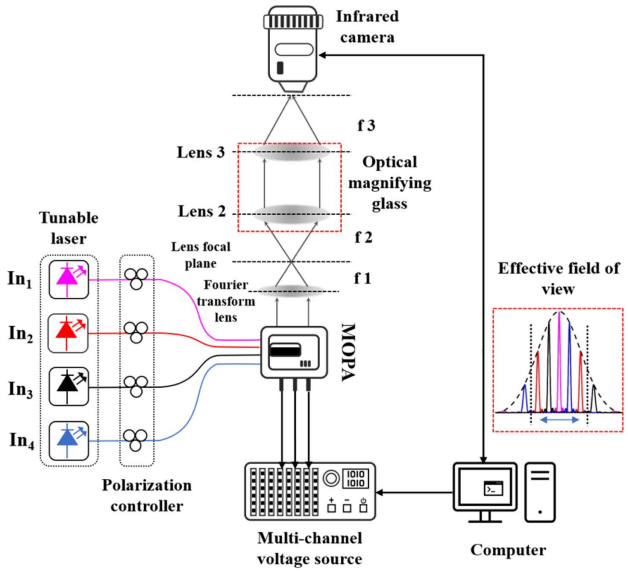

Fig. 6. Schematic diagram of the multi-beam imaging system.

quadratic programming (SQP) algorithm and a golden-selection search algorithm to optimize the voltage applied to the phase shifter automatically. Figure 7(a) shows the single beam steering with a step of 5° in the ±20° range along the phase scanning direction when the input is from In_1. The FWHM beam divergence angle is 3.2° × 3.91°, consistent with the simulation results.

The voltages applied to the BM phase shifters for multi-beam operation were obtained as detailed in Ref. [21]. With all four lasers turned on, a multi-beam pattern spanning an angular range of 44° was observed. Figures 7(b)–7(d) show the lateral steering of the multi-beam pattern. Note that due to the vignette effect at the edges of the FOV, the optical intensity measured by the far-field imaging system is relatively weak at large angles. Moreover, due to the one-wavelength antenna pitch, as the main lobe moves out of the FOV, its aliased lobe moves in from the other edge. In the other dimension, when the laser wavelength was scanned from 1520 to 1570 nm, the multi-beam pattern shifted vertically from −5° to 3°, as shown in Fig. 7(e). Note that due to the wavelength tuning interval being relatively small, the ordinate is enlarged to show the position of each beam better, resulting in slightly blurred results in Fig. 7(e). Additionally, due to the large beam divergence as well as the optical aberration of the far-field imaging system, aliasing grating lobes at −30° and +30° can be partially observed in the measurable FOV simultaneously.

A detailed wavelength dependency analysis is conducted from 1520 to 1570 nm with a step size of 10 nm. Figure 8 presents the beam quality characterization results. It can be seen that the BM-based MOPA possesses wavelength transparency over an optical band from 1520 to 1570 nm. More specifically, the phase relationship between each channel does not change significantly when the wavelength is tuned within this optical band, and the imaging quality of the beam is not affected. Note that due to the FOV limit of the far-field imaging system, especially the optical aberration to the edges, we have demonstrated the wavelength transparency only within the above optical band. Another limitation for the wavelength transparency range originates from the sidewall roughness of the waveguide structure, causing accumulating random variations of effective refractive index along the waveguide interconnect. This, in turn, results in inter-channel optical path variations both inside the Butler matrix and the power distribution network despite strict geometry equality enforced on the design. Therefore, the optimal beam quality can only be achieved for a specific beam at a specific wavelength, limiting the transparent window and the multi-beam consistency.

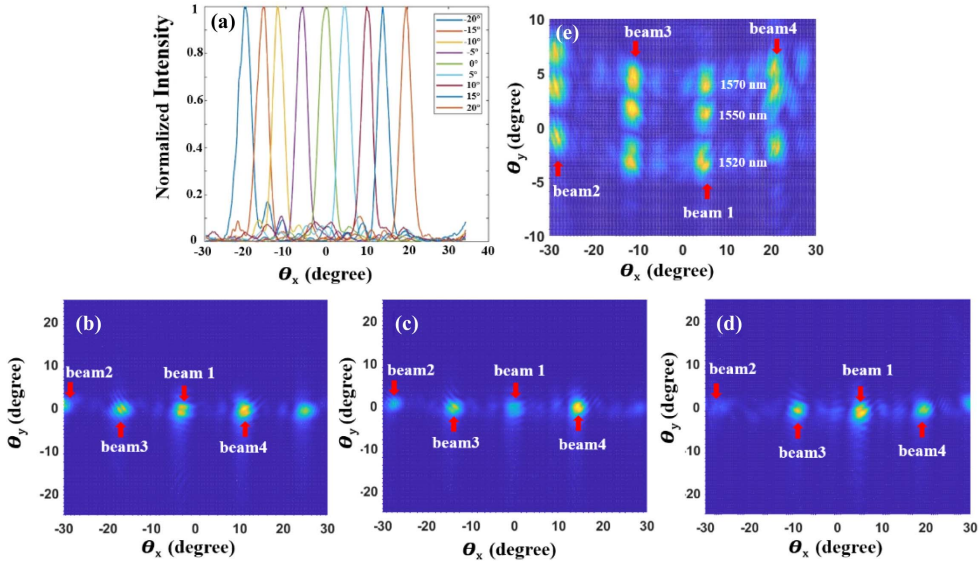

Fig. 7. (a) Normalized far-field intensity distributions in the phase scanning direction of beam1. (b)–(d) Measured multi-beam far-field patterns when beam1 is steered at (b) −5°, (c) 0°, and (d) 5° at the input wavelength of 1550 nm. (e) Measured multi-beam patterns with the input wavelengths at 1520 nm, 1550 nm, and 1570 nm.

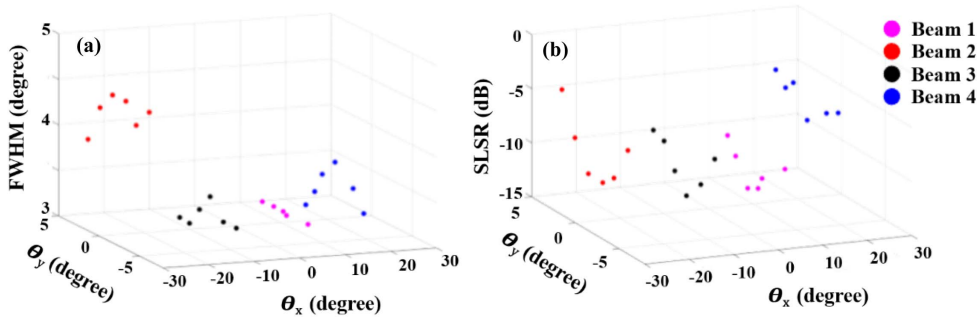

Fig. 8. Results of wavelength transparency validations when the wavelengths of the input lasers of OPA were adjusted sequentially from 1520 to 1570 nm in 10 nm steps. (a) FWHM and (b) SLSR of each beam of the multi-beam OPA.

As a proof of concept, we performed parallel detection and ranging utilizing two linearly frequency chirped lasers simultaneously launched into the MOPA. As shown in Fig. 9, the experimental configuration [28,29] consists of a two-channel arbitrary waveform generator (AWG) to drive two DFB lasers, two erbium-doped fiber amplifiers (EDFAs) to amplify the laser output power, two 9:1 power splitters to distribute optical power between the detection and reference paths, and corresponding polarization and attenuation controllers to optimize the coherent gain. The linearly chirped laser signals are launched into ports In_1 and In_3 of the calibrated MOPA chip, illuminating targets at different angles, whose reflections are then collected with coherent receivers based on avalanche photodetectors (APDs) (Thorlabs APD430C) and free-space components, including caged beam splitters. Note that thanks to the wavelength transparency of the device, we can use different wavelengths for different input ports at the same time with negligible deterioration to the beam quality. Additionally, since the APD also acts as

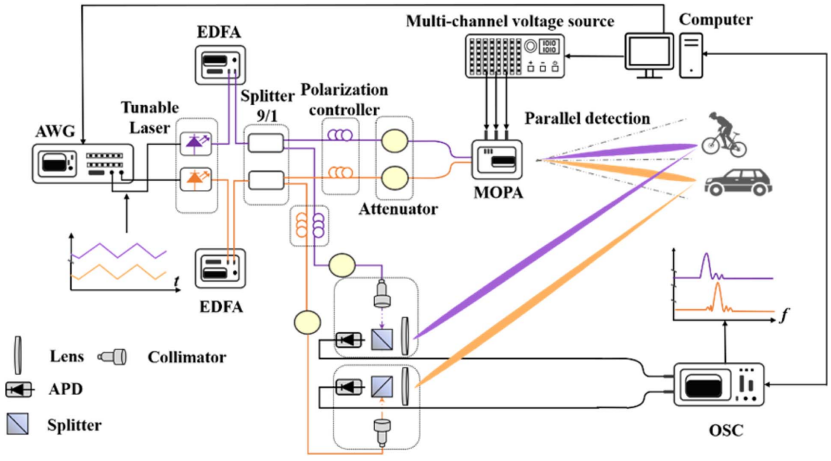

Fig. 9. Schematic diagram of FMCW ranging system. EDFA: erbium-doped fiber amplifier; AWG: arbitrary waveform generator; OSC: oscilloscope; APD: avalanche photodetector.

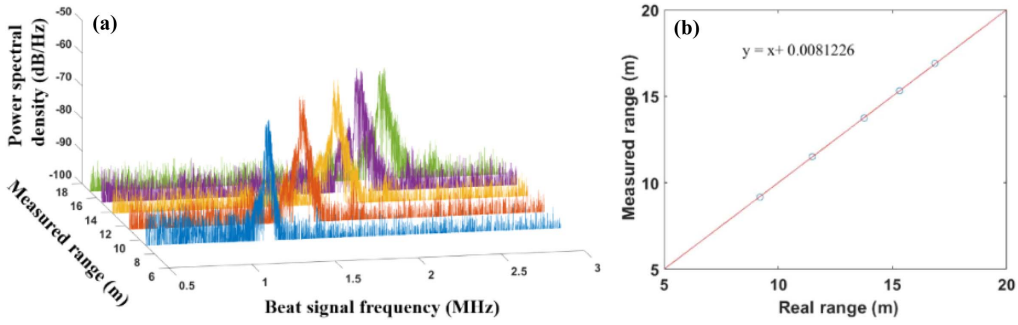

Fig. 10. (a) Power spectral density of the beat signal for a target at the optical path difference of 9.18 m, 11.51 m, 13.74 m, 15.32 m, and 16.91 m. The beam emitting angle is 7.44°. (b) Linear regression of the measured range versus the optical path difference.

a low-pass filter, using chirped signals centered around different operating wavelengths will reject mutual interference between the echo signals. In practice, as long as the wavelength-assisted scanning from different laser sources is not synchronized, i.e., there is no frequency overlap between the chirped signals, simultaneous multi-beam operation can be achieved.

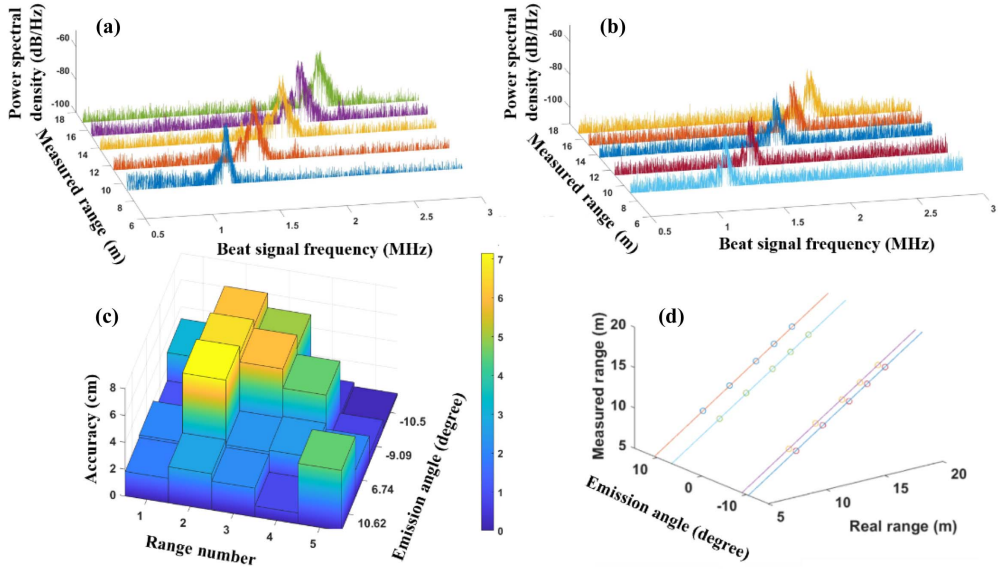

Fig. 11. (a) Power spectral density of beam1 at the emitting angle of 7.44°. (b) Power spectral density of beam3 at the emitting angle of −7.83°. (c) Error summary of multiple ranging experiments. (d) Linear fitting of measured distances with real distances at different angles.

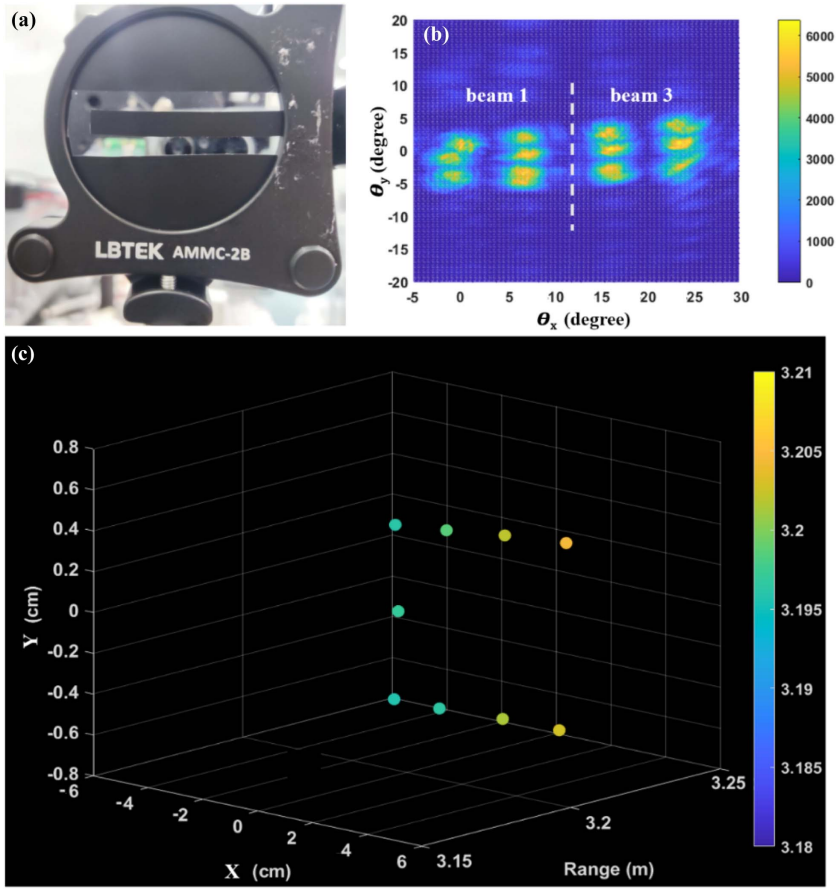

Fig. 12. (a) Picture of the C-shaped target object. (b) Superimposed far-field beam patterns for the scanned beams used for target illumination. (c) Point cloud of the C-shaped target object in the Descartes coordinate system.

To achieve the high linearity required for FMCW ranging, we optimized the DFB driving signal with pre-distortion algorithms, including non-uniform sampling and adaptive linear update, as detailed in our previous work [30]. The achieved linearity is 99.7%, and the chirped bandwidth is about 38.8 GHz. To validate the FMCW ranging of the entire setup, we change the length of the optical fibers in the reference path after free-space alignment of the MOPA transmitter (TX) and coherent receivers (RXs). For example, when beam1 emitting angle is 7.44° at the 1550 nm wavelength, the optical path differences between the free-space detection path and the reference path are 11.51 m, 13.74 m, 15.32 m, and 16.91 m. Meanwhile, the corresponding power spectral density of the beat signals is recorded and shown in Fig. 10(a). Figure 10(b) is a linear regression of the measured range versus the optical path difference and shows the ranging deviation at a single angle.

Similarly, to validate simultaneous FMCW ranging, two beams (beam1 and beam3) are launched through the chip under two operational states. Namely, the MOPA chip is driven with two look-up tables (LUTs) for beamforming at two sets of directions, with beam1 aiming at 7.44° and 4.79° and beam3 aiming at −7.83° and −9.68°, respectively. Therefore, four sets of ranging are conducted for mirrors as target objects at different distances. Note that, for this experiment, the mirrors are relocated each time in free space rather than adjusting the length of the reference path. Figures 11(a) and 11(b) show the power spectral density of the reflected signal from beam1 and beam3 when the emitting angles are 7.44° and −7.83°, respectively. Multi-beam emission and ranging through the same OPA aperture are achieved without additional penalties such as mutual interference. The ranging accuracy w.r.t. the actual range of the four emitting angles is gathered in Fig. 11(c), and the average ranging error is 4 cm. Figure 11(d) represents the fitting diagram of the measured distance and the actual distance at four different emitting angles and five distances for each angle, which can well demonstrate its overall accuracy level.

Finally, we conduct 2D scanning of beam1 and beam3 to image a C-shaped target adapted from a mirror in Fig. 12(a). The target is tilted slightly to demonstrate the ranging capability of the device. In Fig. 12(b), the scanned beams are superimposed in a frame, showing a 3 × 4 grid of 12 points. The two columns of points on the left are emitted by beam1 and the rest by beam3. In the phased-array scanning axis, each point is spaced at about 8°. The DFB laser wavelengths for each row from the top to the bottom are 1570 nm, 1550 nm, and 1530 nm. We show the point cloud of the C-shaped target object in Fig. 12(c).

4. CONCLUSION

We have demonstrated the wavelength transparency of the BM-based MOPA with an emitting aperture composed of grating couplers for wavelength-assisted 2D beam-steering. The MOPA can achieve both beamforming and 2D beam-steering for multiple beams. We also demonstrated parallel multi-beam FMCW ranging with high accuracy for multi-targets without mutual interference. We believe that the demonstration above validates the simultaneous beamforming and beam-steering of multiple beams through a shared grating aperture, which can reduce the system's complexity and improve the sampling rate of solid-state LiDAR systems. To further scale up our device, the number of crossings required will reach a level close to the number of channels. This can be alleviated by replacing the waveguide crossings with overpass crossings developed on the multi-layered Si_3N_4-on-Si platform [31].

Funding. National Key Research and Development Program of China (2022YFB2804502); National Natural Science Foundation of China (6207030193, 62090052, 62135010); Special-Key Project of Innovation Program of Shanghai Municipal Education Commission (2019-07-00-02-E00075).

Disclosures. The authors declare no conflicts of interest.

Data Availability. The data that support the findings of this study are available from the corresponding author upon reasonable request.

REFERENCES

1. F. Zhao, H. Jiang, and Z. Liu, "Recent development of automotive LiDAR technology, industry and trends," Proc. SPIE **11179**, 111794A (2019).
2. Y. Wang, G. Zhou, X. Zhang, *et al.*, "2D broadband beam steering with large-scale MEMS optical phased array," Optica **6**, 557–562 (2019).
3. C. P. Hsu, B. Li, B. Solano-Rivas, *et al.*, "A review and perspective on optical phased array for automotive LiDAR," IEEE J. Sel. Top. Quantum Electron. **27**, 8300416 (2020).
4. Y. Wang, G. Zhou, X. Zhang, *et al.*, "160 × 160 MEMS-based 2-D optical phased array," in *Conference on Lasers and Electro-Optics (CLEO)* (Optica Publishing Group, 2018), paper SM3I.3.
5. X. Zhang, K. Kwon, J. Henriksson, *et al.*, "A large-scale microelectromechanical-systems-based silicon photonics LiDAR," Nature **603**, 253–258 (2022).
6. Y. Guo, Y. Guo, C. Li, *et al.*, "Integrated optical phased arrays for beam forming and steering," Appl. Sci. **11**, 4017 (2021).
7. K. Van Acoleyen, W. Bogaerts, J. Jágerská, *et al.*, "Off-chip beam steering with a one-dimensional optical phased array on silicon-on-insulator," Opt. Lett. **34**, 1477–1479 (2009).
8. J. K. Doylend, M. J. R. Heck, J. T. Bovington, *et al.*, "Two-dimensional free-space beam steering with an optical phased array on silicon-on-insulator," Opt. Express **19**, 21595–21604 (2011).
9. J. C. Hulme, J. K. Doylend, M. J. R. Heck, *et al.*, "Fully integrated hybrid silicon free-space beam steering source with 32-channel phased array," Proc. SPIE **8989**, 898907 (2014).
10. J. Sun, E. Timurdogan, A. Yaacobi, *et al.*, "Large-scale nanophotonic phased array," Nature **493**, 195–199 (2013).
11. Q. Wang, S. Wang, L. Jia, *et al.*, "Silicon nitride assisted 1 × 64 optical phased array based on a SOI platform," Opt. Express **29**, 10509–10517 (2021).
12. J. He, T. Dong, and Y. Xu, "Review of photonic integrated optical phased arrays for space optical communication," IEEE Access **8**, 188284 (2020).
13. R. Fatemi, B. Abiri, A. Khachaturian, *et al.*, "High sensitivity active flat optics optical phased array receiver with a two-dimensional aperture," Opt. Express **26**, 29983–29999 (2018).
14. P. Muñoz, D. Pastor, J. Benítez, *et al.*, "Optical-phased array beam-steering using multi-input slab coupler in silicon nitride waveguides," in *Optical Fiber Communication Conference* (Optica Publishing Group, 2021), paper W1D.
15. Y. Liu, Z. Hao, L. Wang, *et al.*, "On-chip multi-beam emitting optical phased array for wide-angle LIDAR," in *CLEO: Applications and Technology* (Optical Society of America, 2020), paper JTu2G.

16. Y. Wu, S. Shao, and D. Che, "Fast and low grating lobe multi-beam steering with a subarray level unequally spaced optical phased array," J. Opt. Soc. Am. B **38**, 3417–3424 (2021).
17. N. Tyler, D. Fowler, S. Malhouitre, *et al.*, "SiN integrated optical phased arrays for two-dimensional beam steering at a single near-infrared wavelength," Opt. Express **27**, 5851–5858 (2019).
18. L. Wu, X. Wang, X. He, *et al.*, "Arbitrary multiple beam forming by two cascaded liquid crystal optical phased arrays," Opt. Express **26**, 17066–17077 (2018).
19. D. Leonardo, F. Ianni, G. Ruocco, *et al.*, "Computer generation of optimal holograms for optical trap arrays," Opt. Express **15**, 1913–1922 (2007).
20. J. Guo, M. Li, P. Chen, *et al.*, "A multi-beam network based on silicon-based optical waveguide," in *11th UK-Europe-China Workshop on Millimeter Waves and Terahertz Technologies (UCMMT)* (IEEE, 2018), pp. 1–3.
21. P. Lu, W. Xu, C. Zhu, *et al.*, "Integrated multi-beam optical phased array based on a 4 × 4 Butler matrix," Opt. Lett. **46**, 1566–1569 (2021).
22. H. Y. Chi, W. Hong, H. Lai, *et al.*, "Silicon ribbon-based dual-beam optical phased array with low crosstalk and large FoV," Appl. Sci. **12**, 505 (2022).
23. A. Khavasi, L. Chrostowski, Z. Lu, *et al.*, "Significant crosstalk reduction using all-dielectric CMOS-compatible metamaterials," IEEE Photonics Technol. Lett. **28**, 2787–2790 (2016).
24. J. M. Heaton and R. M. Jenkins, "General matrix theory of self-imaging in multi-mode interference (MMI) couplers," IEEE Photonics Technol. Lett. **11**, 212–214 (1999).
25. S. Y. Tseng, C. Fuentes-Hernandez, D. Owens, *et al.*, "Variable splitting ratio 2 × 2 MMI couplers using multi-mode waveguide holograms," Opt. Express **15**, 9015–9021 (2007).
26. R. Nicolas, C. Lukas, V. Raha, *et al.*, "Temperature effects on silicon-on-insulator (SOI) racetrack resonators: a coupled analytic and 2-D finite difference approach," J. Lightwave Technol. **28**, 1380–1391 (2010).
27. Z. Zhou, W. Xu, X. Li, *et al.*, "Butler matrix enabled multi-beam optical phased array for two-dimensional beam-steering," in *27th Opto-Electronics and Communications Conference (OECC) and 2022 International Conference on Photonics in Switching and Computing (PSC)* (IEEE, 2022), pp. 1–3.
28. Y. Li, B. Chen, Q. Na, *et al.*, "Wide-steering-angle high-resolution optical phased array," Photonics Res. **9**, 2511–2518 (2021).
29. J. Zheng, *Optical Frequency-Modulated Continuous-Wave (FMCW) Interferometry* (Springer, 2005).
30. C. Liu, L. Lu, Y. Guo, *et al.*, "Hybrid integrated frequency-modulated continuous-wave laser with synchronous tuning," J. Lightwave Technol. **40**, 5636–5645 (2022).
31. W. D. Sacher, J. C. Mikkelsen, P. Dumais, *et al.*, "Tri-layer silicon nitride-on-silicon photonic platform for ultra-low-loss crossings and interlayer transitions," Opt. Express **25**, 30862–30875 (2017).